



# X-ray Electron Density Study of the Chemical Bonding Origin of Glass Formation in Metal–Organic Frameworks\*\*

Sounak Sarkar, Thomas Bjørn Egede Grønbech, Aref Mamakhel, Martin Bondesgaard, Kuniyoshi Sugimoto, Eiji Nishibori, and Bo Brummerstedt Iversen\*

**Abstract:** Glass-forming metal–organic frameworks (MOFs) have novel applications, but the origin of their peculiar melting behavior is unclear. Here, we report synchrotron X-ray diffraction electron densities of two zeolitic imidazolate frameworks (ZIFs), the glass-forming Zn-ZIF-zni and the isostructural thermally decomposing Co-ZIF-zni. Electron density analysis shows that the Zn–N bonds are more ionic than the Co–N bonds, which have distinct covalent features. Variable-temperature Raman spectra reveal the onset of significant imidazolate bond weakening in Co-ZIF-zni above 673 K. Melting can be controlled by tuning the metal–ligand and imidazole bonding strength as shown from thermal analysis of nine solid-solution  $\text{Co}_x\text{Zn}_{1-x}$ -ZIF-zni ( $x=0.3$  to 0.003) MOFs, and a mere 4% Co-doping into Zn-ZIF-zni results in thermal decomposition instead of melting. The present findings demonstrate the key role of the metal–ligand bonds and imidazolate bonds in controlling the delicate balance between melting and decomposition processes in this class of ZIF compounds.

## Introduction

Metal–organic framework (MOF) materials are usually preferred to be crystalline for straightforward structural characterization using conventional X-ray diffraction techniques. Structural information from long-range crystalline MOFs provides insight that can be used for designing pore size or ligand functionalization for potential applications.<sup>[1]</sup> However, amorphous MOFs<sup>[2]</sup> are increasingly targeted in application e.g. for drug delivery,<sup>[3]</sup> packing and delivery of enzymes,<sup>[4]</sup> or hydrocarbon adsorption<sup>[5]</sup> mostly due to grain-boundary-free nature, isotropic mechanical response and structural flexibility for shape-selective adsorption of compounds with specific dimensions. Pioneering work on amorphous MOFs has especially concerned the MOF family of zeolitic imidazolate frameworks (ZIFs)<sup>[6]</sup> The network topology of ZIFs consists of tetrahedral metal centres (e.g.  $\text{Zn}^{\text{II}}$ ,  $\text{Co}^{\text{II}}$ ) connected by imidazolate linkers, which replicates the building block of corner sharing  $\text{SiO}_4$  tetrahedra in zeolites (Figure 1). Contrary to the majority of MOFs that show thermal decomposition upon heating, several members of the ZIF family melt above 400 °C,<sup>[7]</sup> and they form glasses when thermally quenched from the molten state. Glass-

[\*] Dr. S. Sarkar, T. B. E. Grønbech, Dr. A. Mamakhel, Dr. M. Bondesgaard, Prof. B. B. Iversen  
 Center for Materials Crystallography, Department of Chemistry and Interdisciplinary Nanoscience Center (iNANO), Aarhus University, Langelandsgade 140, 8000 Aarhus (Denmark)  
 E-mail: bo@chem.au.dk

Prof. K. Sugimoto  
 Japan Synchrotron Radiation Research Institute (JASRI),  
 1-1-1 Kouto, Sayo-cho, Sayo-gun, Hyogo 679-5198 (Japan)

Prof. E. Nishibori  
 Faculty of Pure and Applied Sciences, Tsukuba Research Center for Energy Materials Science (TREMS), University of Tsukuba,  
 1-1-1 Tennodai, Tsukuba, Ibaraki 305-8571 (Japan)

[\*\*] A previous version of this manuscript has been deposited on a preprint server (<https://doi.org/10.26434/chemrxiv-2022-wszv7>).

© 2022 The Authors. Angewandte Chemie International Edition published by Wiley-VCH GmbH. This is an open access article under the terms of the Creative Commons Attribution Non-Commercial NoDerivs License, which permits use and distribution in any medium, provided the original work is properly cited, the use is non-commercial and no modifications or adaptations are made.

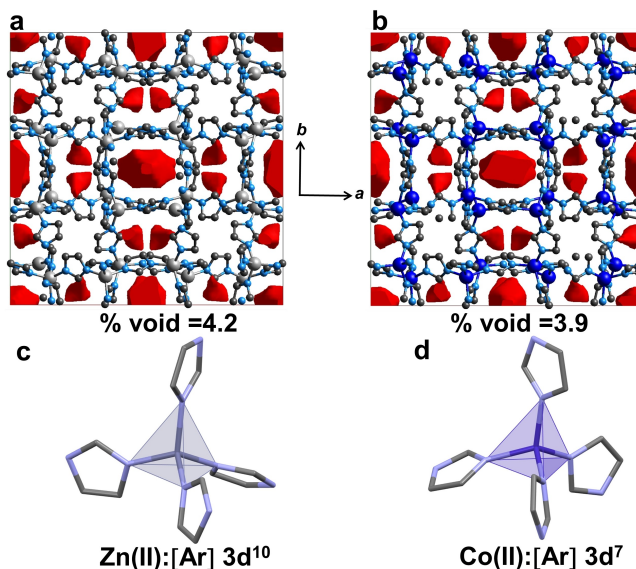


**Figure 1.** Top: Unit cell packing with voids<sup>[26]</sup> (red surfaces) viewed along the *c* axis of unit cell in a) Zn-ZIF-zni<sup>[27]</sup> and b) Co-ZIF-zni.<sup>[27]</sup> Bottom: Building unit of ZIF-zni with c)  $\text{Zn}^{\text{II}}$  and d)  $\text{Co}^{\text{II}}$  in a tetrahedral coordination with four crystallographic independent imidazolate rings.

forming ZIFs have opened up new avenues of fundamental and applied research.<sup>[8]</sup> Pure ZIF glasses as well as fabricated glass membranes with intrinsic permanent porosity are investigated as potential materials for gas mixture separations ( $\text{H}_2/\text{CH}_4$ ,  $\text{CO}_2/\text{N}_2$ , and  $\text{CO}_2/\text{CH}_4$ , propane, propylene, and n-butane)<sup>[9]</sup> and  $\text{CO}_2$  adsorption.<sup>[10]</sup> ZIF glasses are also being explored as candidates for optical luminescence materials,<sup>[11]</sup> non-linear optical materials,<sup>[12]</sup> quasi-solid-state-electrolytes,<sup>[13]</sup> anode material in lithium-ion batteries<sup>[14]</sup> or electrodes for oxygen evolution reaction.<sup>[15]</sup> Notably, ZIF glasses offer better processability for bulk application than crystalline powders.<sup>[16]</sup>

The archetypical ZIF-4 material containing  $\text{Zn}^{2+}$  ions was the first observed glass-forming MOF.<sup>[17]</sup> Coudert et al. used first-principle molecular dynamics (MD) simulation and a combination of neutron and X-ray pair distribution function analysis to demonstrate that melting of Zn-ZIF-4 involves rapid fluctuations between three-coordinated and four-coordinated Zn-imidazolate units at picosecond time scale.<sup>[18]</sup> Comparative MD simulation studies between ZIF-4 and highly porous ZIF-8 further shows that the melting tendency of MOFs is dependent on the characteristic framework topology.<sup>[19]</sup>

Interestingly, the isostructural Co-ZIF-4 material decomposes without melting under heat treatment. Zn-ZIF-4 and Co-ZIF-4 have similar thermal signatures when heated in an argon atmosphere with solvent loss from the lattice around 220 °C, followed by amorphization above 300 °C, and eventual recrystallization at about 370–400 °C to the densest ZIF polymorph, the so-called ZIF-zni.<sup>[20]</sup> Melting of Zn-ZIF-zni is observed at 590 °C followed by decomposition above 600 °C (Figure S1a). In contrast, Co-ZIF-zni decomposes at 530 °C (Figure S1b). It is puzzling why these two isostructural ZIFs, Zn-ZIF-zni and Co-ZIF-zni, behave fundamentally different upon heating. They differ only in the electronic configuration of their transition metal center with closed shell  $d^{10}$  for  $\text{Zn}^{\text{II}}$  and open shell  $d^7$  for  $\text{Co}^{\text{II}}$ . This suggests that the thermal stability of these individual MOFs and hence their glass-forming ability is correlated to the nature of the metal-ligand bonding.

Various empirical design strategies based on mixed-ligand approaches have been pursued to lower the melting point temperature of ZIF-62 (and derivatives), whose structures are isomorphous to ZIF-4.<sup>[9b,21]</sup> However, to date, the physicochemical origin of the melting behaviors remains poorly understood. When addressing the correlation between the melting/decomposition process and the metal-ligand bonding in Zn-ZIF/Co-ZIF, two questions appear important: i) how does the nature of the Zn–ligand bond compare to the Co–ligand bond? and ii) what is the impact of this difference on the structural dynamics and bond strength (stability) of imidazolate linkers in different ZIFs? Here we address the questions based on analyses of electron density (ED) distributions obtained from modelling of very accurate 25 K synchrotron X-ray diffraction data measured to a high resolution of  $\sin\theta/\lambda = 1.35 \text{ \AA}^{-1}$  and  $1.25 \text{ \AA}^{-1}$  for Zn-ZIF-zni and Co-ZIF-zni respectively. ED analysis provides detailed information on chemical bonding and it has helped to form an understanding of structure–property relationships

in material research.<sup>[22]</sup> However, ED studies of MOF materials remain a severe challenge both for experimental (X-ray diffraction) and computational (ab initio) methods. The possible presence of disordered solvents in the pores, framework disorder or large atomic displacements in the flexible linkers hinders accurate modelling of X-ray structure factors, while large open shell extended molecular systems with magnetic ordering are computationally costly and suffer convergence issues. In a few cases, use of intense high-energy synchrotron X-ray radiation in combination with area detector technology has resulted in experimental ED studies of MOFs.<sup>[23]</sup>

We have determined accurate EDs of Zn-ZIF-zni and Co-ZIF-zni based on multipole modelling<sup>[24]</sup> of 25 K single-crystal synchrotron X-ray diffraction data (Table 1) supplemented with periodic DFT calculations. ZIF-zni, the highest density polymorph was selected for this study because its crystal structure is devoid of solvents, thus avoiding potential structural disorder. Similar to ZIF-4, other ZIFs such as ZIF-1, ZIF-3, ZIF-zeg, and ZIF-nog, also undergo thermal amorphization and recrystallization to ZIF-zni prior to melting/decomposition.<sup>[20,25]</sup> To complement the X-ray ED data we have collected multi-temperature (25–400 K) single-crystal X-ray diffraction data for structural analysis as well as multi-temperature (300–773 K) Raman spectroscopy data to investigate the structural changes in the ZIF-zni frameworks during heating. Finally, the thermal behavior of a series of nine solid solutions of  $\text{Co}_x\text{Zn}_{1-x}$ -ZIF-zni ( $x$  ranging from 0.3 to 0.003) was analyzed by simultaneous thermogravimetric analysis and differential scanning calorimetry (TGA and DSC) to further probe the role of metal-ligand bonding in regulating the melting/decomposition process in ZIFs.

## Results and Discussion

The dense Zn and Co ZIF-zni MOFs (void volume is only  $\approx 4\%$  of the unit cells) are isostructural and they belong to the tetragonal  $I4_1cd$  space group (Table S1). In the asymmetric unit of both crystal structures, two symmetry independent metal centres form a distorted tetrahedral with four imidazolate rings in a 1:2 stoichiometry (Figure 1 and Figure S7). The N atoms of the imidazolate ligands are coordinated to the respective metal centres. The metal–nitrogen (M–N) bond lengths (mean value  $\approx 1.985 \text{ \AA}$ , Table S2) and  $\angle\text{N–M–N}$  bonds angles (mean value  $\approx 109.6^\circ$ , Table S3) in both 25 K crystal structures are very similar, but differences in the electron configurations of the metal ions may affect the nature and strength of the chemical bonding between the metals and the ligands.

To obtain accurate ED models of the two ZIFs, several models were tested and the residual density was scrutinized for systematic features. In addition, the monopole populations of the metal atoms was checked to avoid unphysical results. The multipole models with lowest residual density peaks/holes ( $\approx 0.4/-0.4 \text{ e\AA}^{-3}$  for Zn-ZIF-zni,  $\approx 0.3/-0.4 \text{ e\AA}^{-3}$  for Co-ZIF-zni) are considered for bonding analysis. Such low ED residuals in MOF structures signifies

**Table 1:** Topological analysis at bond critical points (BCPs) of metal–N bonds from experimental multipole model (first line) and periodic DFT calculations (second line in italics).  $R$  is the bond path length, which is a gradient trajectory length originating at the BCP and terminating at the nuclei (Figure S10).  $\rho$  and  $\nabla^2\rho$  are the electron density and its Laplacian, respectively.  $G_b$ ,  $V_b$  and  $H_b$  are the kinetic, potential and total energy density ( $H_b = G_b + V_b$ ) at the BCP, respectively.  $H_b/\rho$  and  $G_b/\rho$  are in atomic units (a.u.).  $\epsilon$  is the bond ellipticity [ $\epsilon = (\lambda_1/\lambda_2) - 1$ ] defined as the ratio of the eigenvalues  $\lambda_1$  and  $\lambda_2$  of the Hessian matrix. These values correspond to the negative curvature of electron density along two perpendicular directions to the bond path.

Bonds	$R$ [Å]	$\rho$ [ $\text{e}\text{\AA}^{-3}$ ]	$\nabla^2\rho$ [ $\text{e}\text{\AA}^{-3}$ ]	$\epsilon$	$G_b/\rho$	$ V_b /G_b$	$H_b/\rho$
Zn1–N4	1.991	0.533	9.526	0.08	1.36	1.08	−0.11
	<i>1.991</i>	<i>0.606</i>	<i>8.812</i>	<i>0.06</i>	<i>1.26</i>	<i>1.19</i>	<i>−0.24</i>
Co1–N4	1.994	0.678	9.808	0.11	1.30	1.22	−0.28
	<i>1.993</i>	<i>0.619</i>	<i>8.362</i>	<i>0.07</i>	<i>1.22</i>	<i>1.22</i>	<i>−0.27</i>
Zn1–N6	1.987	0.512	9.808	0.09	1.41	1.05	−0.07
	<i>1.986</i>	<i>0.612</i>	<i>8.931</i>	<i>0.05</i>	<i>1.26</i>	<i>1.19</i>	<i>−0.24</i>
Co1–N6	1.987	0.714	10.493	0.09	1.33	1.22	−0.30
	<i>1.987</i>	<i>0.626</i>	<i>8.595</i>	<i>0.03</i>	<i>1.23</i>	<i>1.22</i>	<i>−0.27</i>
Zn2–N3	1.995	0.528	9.961	0.08	1.41	1.06	−0.08
	<i>1.995</i>	<i>0.602</i>	<i>8.746</i>	<i>0.06</i>	<i>1.25</i>	<i>1.19</i>	<i>−0.23</i>
Co2–N3	1.990	0.719	9.669	0.09	1.27	1.26	−0.33
	<i>1.989</i>	<i>0.624</i>	<i>8.393</i>	<i>0.08</i>	<i>1.22</i>	<i>1.22</i>	<i>−0.27</i>
Zn2–N7	1.979	0.564	10.471	0.09	1.42	1.08	−0.12
	<i>1.979</i>	<i>0.622</i>	<i>9.184</i>	<i>0.05</i>	<i>1.28</i>	<i>1.19</i>	<i>−0.24</i>
Co2–N7	1.987	0.673	10.652	0.09	1.36	1.18	−0.25
	<i>1.981</i>	<i>0.635</i>	<i>8.732</i>	<i>0.05</i>	<i>1.25</i>	<i>1.22</i>	<i>−0.27</i>

accuracy of the respective charge density models. Details of the multipole modelling of the X-ray structure factors to obtain the experimental EDs are provided in the Supporting Information.

The d-orbital populations of the Co atoms derived from experimental ED fits well with their distorted tetrahedral geometry showing a preferential occupancy in  $d_{xy}$  orbitals compared to  $d_{yz}$  and  $d_{zx}$  (Table S4). The experimental static deformation densities,  $\rho_{\text{def}} = \rho_{\text{model}} - \rho_{\text{IAM}}$ , reveal details about the metal–N bonds (Figure 2). Here IAM refers to Independent Atom Model, i.e. the electron density of spherical neutral gas phase atoms placed at the unit cell positions. This is the model typically used in structural analysis in X-ray crystallography and it represents the reference state in which there is no chemical bonding between the atoms. The deformation maps, show aspherical ED features on Zn

metal centres, i.e. a pronounced deviation from the expected spherical  $3d^{10}$  density of a Zn atom. The lone pair in the valence shell charge concentration (VSCC) region of N atoms along the N–Zn–N plane (blue contours in 2D map and blue lumps in 3D maps) are polarized toward the charge concentration regions of the Zn atoms. In contrast to the Zn–N bonding, there is a strong overlap between the lone pairs in the VSCC of N and Co orbitals leading to ED accumulation in Co–N bonds. This suggests significant covalency in these bonds similar to the features observed in deformation densities of the C–N and C–C bonds in the imidazolate rings (Figure S9).

To quantify the metal–ligand bonding we use topological analysis based on QTAIM theory,<sup>[28]</sup> and we compare EDs obtained from experiments as well as single point periodic DFT calculations in the experimental geometry (Table 1 and Table S7). Although the bond path lengths ( $R$ ) are indistinguishable between the two structures, the Zn–N bonds have lower experimental electron density ( $\rho$ ) values (0.51–0.57  $\text{e}\text{\AA}^{-3}$ ) at the bond critical points (BCPs) compared with the Co–N bonds (0.60–0.72  $\text{e}\text{\AA}^{-3}$ ). This corroborates the charge accumulation between Co and N observed in the static deformation maps (Figure 2). The positive Laplacian values ( $\nabla^2\rho$ ) at the BCPs are typical of metal–ligand bonding<sup>[29]</sup> but we do not observe a clear trend in the experimental values for the Zn–N and Co–N bonds presumably due to experimental noise (see Supporting Information, Figure S2 and Figure S4). The theoretical Laplacian values are consistently less positive in Co–N bonds than Zn–N bonds corroborating a more covalent character in the former. The local kinetic ( $G_b$ ), potential ( $V_b$ ) and total energy ( $H_b$ ) densities evaluated at the BCPs characterize the metal–ligand interactions as a mixture of closed/shared shell interactions generally observed in transition metal coordination complexes.<sup>[29,30]</sup> The kinetic energy per electron ( $G_b/\rho$ )

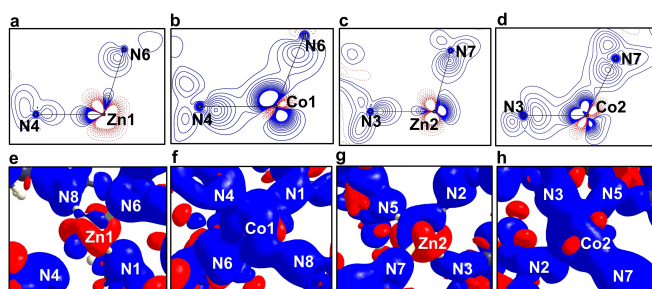


**Figure 2.** 2D static deformation density in the plane of N–M–N for a, c) Zn-ZIF-zni, b, d) Co-ZIF-zni. Blue solid lines and red dots represents positive and negative contours, respectively, and the contour level is  $\pm 0.1 \text{ e}\text{\AA}^{-3}$ . e–h) 3D static deformation density of  $\text{MN}_4$  tetrahedra for e, g) Zn-ZIF-zni, f, h) Co-ZIF-zni. Blue regions indicate the charge concentration regions, while red regions indicate charge-depleted regions and the contour level is  $\pm 0.1 \text{ e}\text{\AA}^{-3}$ .

is slightly higher in the Zn–N bonds, which corroborates their more ionic nature. The dominance of potential energy manifested by increased  $|V_b|/G_b$  ratios and larger negative total energy per electron ( $H_b/\rho$ ) at the BCPs show that the Co–N bonds have more covalent character than the Zn–N bonds. It is interesting to note that differences in the topological parameters ( $\rho$ ,  $G_b/\rho$ ,  $|V_b|/G_b$ ,  $H_b/\rho$ ) at BCPs of metal–ligand bond between Zn-ZIF-zni and Co-ZIF-zni are more prominent in the experimental model as compared to the theoretical model, thereby underpinning the importance of experimental benchmark for testing theoretical studies of chemical bonding in extended structures.<sup>[31]</sup> This quantification of ionicity and covalence in the respective metal–ligand bonds is instrumental in investigating the difference in the thermal stability of Zn-ZIF-zni and Co-ZIF-zni as discussed latter in the paper. We emphasize the necessity of quantitative chemical bonding analysis rather than bonding assessment based on simple chemical concepts when discussing structure-property correlations in materials. Indeed, studies on thermoelectric  $Mg_3Sb_2$ ,<sup>[32]</sup> or half-Huesler semiconductors<sup>[33]</sup> have challenged the validity of simple bonding theories such as the Zintl concept to describe chemical bonding.

Further, we calculated the total density of states (DOS) and projected density of states (PDOS) of Zn-ZIF-zni and Co-ZIF-zni as shown in Figure S11 and Figure S12. In Zn-ZIF-zni, analysis of the individual atomic orbital's PDOS reveals that the valence bands (VB) near the Fermi level largely consist of ligand atoms with negligible participation from the Zn atoms (Figure S11). On the contrary, the Co 3d orbitals below the Fermi level forms narrow and broad bands in Co-ZIF-zni (Figure S12). The broad bonding bands due to clear mixing of 3d states of Co atoms and 2p states of C, N atoms in the VB region account for the partial covalent character of Co–N bonds and also hint at the possibility of  $\pi$ -backbonding interactions between Co and imidazolate ligands.

The difference in the nature of chemical bonding impacts the thermal vibrations of the metal and N atoms in the respective ZIFs. The evolution of atomic displacement parameters (ADP) with increasing temperature provide insights into the structural dynamics<sup>[34]</sup> and therefore information relevant to the thermal stabilities of Zn/Co-ZIF-zni. We have collected synchrotron single-crystal X-ray diffraction data for structural analysis for Zn-ZIF-zni and Co-ZIF-zni at temperatures of 25 K, 100 K, 200 K, 300 K and 400 K. The mean equivalent isotropic ADPs of the metals ( $U_{eq}^M$ ), N atoms ( $U_{eq}^N$ ) and C atoms ( $U_{eq}^C$ ) are compared for all temperatures (Figure S13). The Zn atoms have larger ADPs than the Co atoms reflecting the stiffer covalent Co–N bonds, which restrict the movement of the Co atoms. Not surprisingly, the ADPs of the N and C atoms in the imidazolate rings are higher than for the metals (lighter mass). The equivalent isotropic ADPs ( $U_{eq}$ ) of ring C atoms (Figure S14) and the rate of change of the ADPs with temperature (Figure S15) indicate that the C1 and C2 atoms of ring 1 and C4 and C5 atoms of ring 2 display very pronounced out-of-plane libration similar to the benzene ring in MOF-5.<sup>[34]</sup> This reflects significant local distortion of

the imidazolate ring with increasing temperature, where the upper part of the ring (M1–N–C–N–M2) vibrates less out-of-plane than the lower part (–C–C–).

To probe the distortion of the frameworks at a molecular level, the ratio of  $U_{eq}$  values of ring C atom and its nearest neighbour metal atom (Zn, Co) is calculated as  $R_d = U_{eq}(\text{Zn, Co})/U_{eq}(\text{C})$ . The nitrogen atoms are excluded from this parameter because they are bonded to both C and M atoms and hence can introduce biases to this analysis.  $R_d$  is an estimate of difference in thermal vibration between the metal atoms and the imidazolate rings, and it is an indirect measure of the framework distortion (see Figure 3). Beyond 200 K, the ADPs of the “lower ring” C1 and C2 increases strongly compared with Zn and Co atoms, whereas the ADP of the C3 atom bonded to two nitrogens largely follow the trend of the metal ( $dU_{eq}(\text{C3})/dT \approx 1.9 \times 10^{-4} \text{ \AA}^2 \text{ K}^{-1}$ ,  $dU_{eq}(\text{Zn, Co})/dT \approx 1.4 \times 10^{-4} \text{ \AA}^2 \text{ K}^{-1}$ , Figure S16, Figure S17). Comparison of  $R_d$  values across all temperatures reveal larger difference in ADPs between the tightly bound Co and the flexible C atoms of ring 1 than for Zn and a similar trend is seen for the Co atom and the C atoms of the other imidazolate rings (Figure S18, S19 and S20). Co-ZIF-zni clearly exhibits greater framework distortion during heating to 400 K and therefore have lower thermal stability than Zn-ZIF-zni.

It was not possible to study the structural changes beyond 400 K using single-crystal X-ray crystallography due to deterioration in data quality. Instead, multi-temperature Raman spectroscopy was employed to indirectly follow structural changes. Sun et al. used temperature dependent

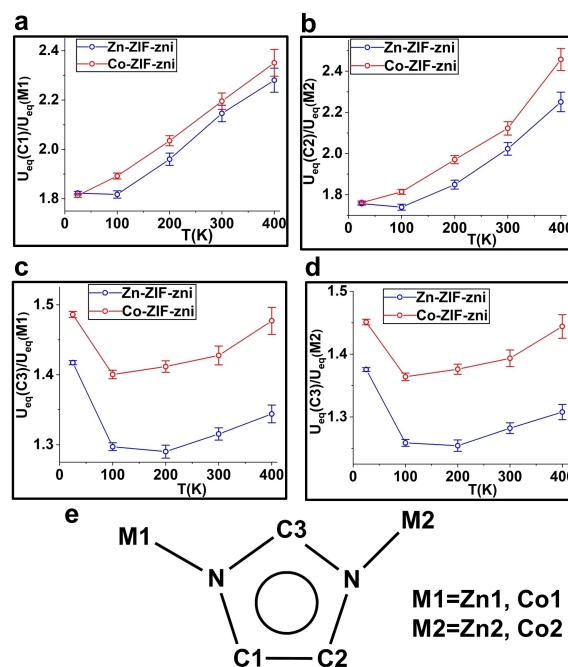


**Figure 3.** a–d) Comparison of temperature-dependent variation in  $R_d$  (ratio of  $U_{eq}$  values of C atoms of ring 1 (e) and its nearest neighbour Zn/Co) based on variable temperature (25–400 K) synchrotron X-ray diffraction data. e) Molecular diagram of ring 1 bonded with Zn/Co metals.

Fourier transform infrared (FTIR) spectroscopy to study the thermolysis mechanism of isostructural ZIF-8 (Zn) and ZIF-67 (Co) MOFs.<sup>[35]</sup> Here Raman spectra were recorded from 300 K to 773 K/823 K under nitrogen flow in the range of 1100–1600  $\text{cm}^{-1}$ . The signature peaks of Zn–N/Co–N bonds were too weak to detect in the lower wavenumber region (below 300  $\text{cm}^{-1}$ ). The major peaks are assigned<sup>[36]</sup> to the following modes in imidazolate ring-symmetric stretch of longer C–N bonds [ $\nu_s(\text{C1N1}, \text{C2N2})$ , (1145–1177  $\text{cm}^{-1}$ )], symmetric stretch of shorter C–N bonds in N–C–N linkage [ $\nu_s(\text{C3N1}, \text{C3N2})$ , (1255–1284  $\text{cm}^{-1}$ )] and C=C bond stretching [ $\nu_s(\text{C1C2})$ , (1490–1495  $\text{cm}^{-1}$ )] (Figure S21). The Raman peaks broaden with increasing temperature and the peak positions shift to lower wavenumbers because of lattice expansion. Beyond 700 K, the peak intensities in Co-ZIF-zni drastically reduce and identification of the weaker C=C Raman band becomes difficult.

The symmetric stretching modes [ $\nu_s(\text{C1N1}, \text{C2N2})$ ,  $\nu_s(\text{C3N1}, \text{C3N2})$ ] in the imidazolate rings of Co-ZIF-zni have lower frequencies than in Zn-ZIF-zni at all temperatures indicating weaker bonds in the former MOF (Figure 4, ring 1 is a representative example for all imidazolate linkers). This observation emphasizes the implicit role of  $\pi$ -backbonding interaction between Co and ligands for weakening the imidazolate bonds of Co-ZIF-zni. The two characteristic C–N stretching modes in Zn-ZIF-zni exhibit a smooth red shift from 1176  $\text{cm}^{-1}$  to 1163  $\text{cm}^{-1}$  and from 1284  $\text{cm}^{-1}$  to 1273  $\text{cm}^{-1}$  during heating. In contrast, the shift of peak positions (1167  $\text{cm}^{-1}$  to 1144  $\text{cm}^{-1}$ , 1277  $\text{cm}^{-1}$  to 1255  $\text{cm}^{-1}$ ) is discontinuous in Co-ZIF-zni, particularly the  $\nu_s(\text{C3N1}, \text{C3N2})$  modes show inflection beyond 673 K. This suggests strong ring deformation prior to imidazolate bond dissociation in Co-ZIF-zni as the temperature approaches decomposition point (803 K, Figure S1b). In Zn-ZIF-zni, the C–N Raman peaks are observed up to 823 K (Figure S21), i.e. close to melting point ( $\approx 860$  K), suggesting that the

imidazolate rings remain intact in the melted form due to relatively stronger imidazolate bonds.

In order to further probe the role of the metal–N bonds on the thermal behavior of these ZIF compounds, we prepared a series of nine solid solution (SS) materials,  $\text{Co}_x\text{Zn}_{1-x}$ -ZIF-zni, where the Co mole fraction ( $x$ ) ranges from 0.3 to as low as 0.003. The final stoichiometry for each SS was determined from Inductively Coupled Plasma Optical Emission Spectrometry (ICP-OES) analysis (Table S11). TGA coupled with DSC measurements were done by heating the SS samples to 750  $^\circ\text{C}$  in argon at a rate of 10  $\text{K min}^{-1}$  to analyze their thermal behavior. The phase diagram for all SS materials is presented in Figure 5 based on DSC-TGA measurements.  $T_m$  is the offset temperature of the endothermic peak in DSC profile, while  $T_d$  is the onset decomposition temperature deduced from TGA graphs (Figure S22).

We observe a systematic dependence of thermal stability of  $\text{Co}_x\text{Zn}_{1-x}$ -ZIF-zni SS phases on percentage of Co doping in the crystal structure (Figure 5a). In the mole fraction range of 0.3–0.04 Co,  $T_d$  is lower than  $T_m$  ( $\approx 7$ –21  $^\circ\text{C}$ ) suggesting decomposition for these SS materials. Thus, even a very low quantity of Co dopant ( $\approx 4\%$ ) fundamentally alters the thermal stability with respect to the parent Zn-ZIF-zni structure. At ultralow mole fractions of Co ( $x=0.01$  to 0.003) in  $\text{Co}_x\text{Zn}_{1-x}$ -ZIF-zni, sharp endothermic peaks of melting are observed as the corresponding  $T_m$  values are lower than  $T_d$  values by  $\approx 11$   $^\circ\text{C}$ . The melting behavior is observed macroscopically where the melted SS compounds lose their needle-like morphology compared with decomposed SS samples (Figure 5b,c). In separate experiment, these three  $\text{Co}_x\text{Zn}_{1-x}$ -ZIF-zni ( $x=0.01$  to 0.003) SS crystalline samples were heated up to their  $T_m$  and then cooled back to room temperature to form melt-quenched hybrid glass (see powder X-ray diffraction patterns, Figure S23). The melt-quenched samples are termed as  $a_g\text{Co}_{0.010}\text{Zn}_{0.990}$ -

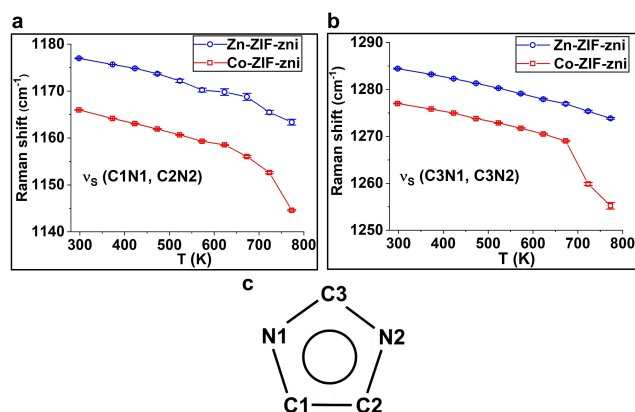


**Figure 4.** Comparison of temperature-dependent variation in Raman peak shifting corresponding to a) symmetric stretch of longer C–N bonds (C1–N1 and C2–N2 bonds, 1145–1177  $\text{cm}^{-1}$ ) and b) symmetric stretch of shorter C–N bonds in N–C–N linkage (C3–N1 and C3–N2 bonds, 1255–1284  $\text{cm}^{-1}$ ) of imidazolate rings. c) Molecular diagram of ring 1 as a representative example for all imidazolate linkers.

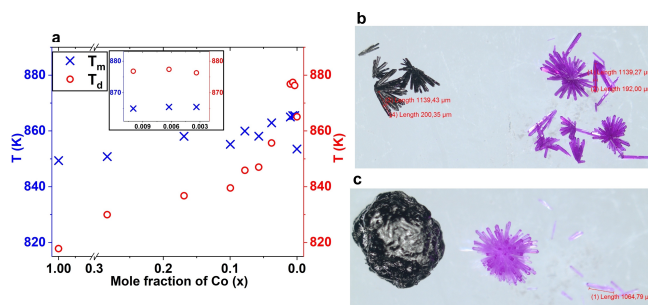


**Figure 5.** Phase diagram of  $\text{Co}_x\text{Zn}_{1-x}$ -ZIF-zni ( $x=0.3$  to 0.003) solid solutions and the parent ZIFs-Co-ZIF-zni ( $x=1$ ) Zn-ZIF-zni ( $x=0$ ).  $T_m$  is the offset temperature of the calorimetric melting peak in DSC plots, while  $T_d$  is the extrapolated onset decomposition temperature on the TGA curves (Figure S22) obtained from simultaneous TGS/DSC experiments. The respective  $T_m$  and  $T_d$  for the ultralow mole fractions of Co ( $x=0.01$  to 0.003) in  $\text{Co}_x\text{Zn}_{1-x}$ -ZIF-zni is shown in inset. Optical images of two solid-solution samples b)  $\text{Co}_{0.04}\text{Zn}_{0.96}$ -ZIF-zni, c)  $\text{Co}_{0.01}\text{Zn}_{0.99}$ -ZIF-zni before heating (right-purple crystals) and after heating (left-black product) in an argon atmosphere up to 750  $^\circ\text{C}$ . The scale of individual images is 200  $\mu\text{m}$ .

ZIF-zni,  $a_g\text{Co}_{0.006}\text{Zn}_{0.994}\text{-ZIF-zni}$  and  $a_g\text{Co}_{0.003}\text{Zn}_{0.997}\text{-ZIF-zni}$ . The corresponding glass transition temperature ( $T_g$ ) of these melt quenched SS ZIFs are observed in the range of 558–568 K from the DSC experiments with a heating rate of  $10\text{ K min}^{-1}$  (Figure S24).

It is intriguing that a few percent of Co atoms in Zn-ZIF-zni is able to disrupt the lattice and cause decomposition. Hence, in a cluster of  $3\times 3\times 3$  Zn atoms in the Zn-ZIF-zni lattice mimicking 4 % doped Co SS phase, substitution of one Zn by Co causes chemical disruption and decomposition (Figure S25). This implies that the “correlation length” of the local chemical bonding consisting of at least a trimer of metal atoms which extends for about 8–11 Å in Zn-ZIF-zni. To rephrase it, a theoretical cluster calculation would not represent the Zn-ZIF-zni chemical bonding if not containing at least  $4\times 4\times 4$  Zn atoms.

## Conclusion

In summary, using high-resolution synchrotron X-ray diffraction data, for the first time, we have determined accurate EDs of a meltable MOF, Zn-ZIF-zni and the isostructural Co-ZIF-zni, which decomposes upon heating. Static ED deformation maps and quantitative chemical bonding analysis using several topological parameters ( $\rho$ ,  $G_b/\rho$ ,  $|V_b|/G_b$ ,  $H_b/\rho$ ) reveal that for Co-ZIF-zni, the Co–N bonds have distinct covalent features, whereas the Zn–N bonds in Zn-ZIF-zni are more ionic. This is furthermore corroborated by band structure calculations, which shows covalent mixing between the valence states of C, N atoms and the 3d orbitals of Co atoms in Co-ZIF-zni. Temperature-dependent Raman spectroscopy shows that the imidazolate bonds in Zn-ZIF-zni are relatively more stable than in Co-ZIF-zni, which shows an abrupt bond weakening above 673 K. The inherently weaker imidazolate bonds in Co-ZIF-zni could be related to subtle  $\pi$ -backbonding between Co and imidazolate ligands. Multi-temperature X-ray diffraction data corroborate that the thermally induced framework distortion is smaller in Zn-ZIF-zni compared with Co-ZIF-zni. The thermal decomposition versus melting behavior was studied in a series of Co-substituted Zn-ZIF-zni solid solution phases. Even a very low Co concentration of  $\approx 4\%$  leads to disruption of the Zn-ZIF crystal lattice causing a fundamental change in its thermal behavior. It appears that the relatively more ionic Zn–N bond and more stable imidazolate linkers facilitate melting in Zn-ZIF-zni. In contrast, the more directional covalent Co–N bonding, and resultant weakened imidazolate bonding, leads to decomposition in Co-ZIF-zni. The dependency on pore size and framework topology in melting of dense ZIF-4 was hypothesized by first-principle MD simulation studies.<sup>[19]</sup> In addition to these structural factors, we have identified the important roles of metal–ligand bonds and the strength of internal bonds in the linker molecule in controlling the subtle balance between melting and decomposition process. Overall, there appears to be considerable chemical space for example through ligand functionalization or choice of metal to design new MOF glasses.

## Acknowledgements

Funding from the Villum Foundation is gratefully acknowledged. The work was partly supported by the Japan Society for the Promotion of Science (JSPS) Grants-in-Aid for Scientific Research (KAKENHI) Grant Numbers JP19KK0132, JP20H4656, JP21H05235. The synchrotron experiments were performed at SPring-8 BL02B1, Japan, with the approval of the Japan Synchrotron Radiation Research Institute (JASRI) as a Partner User (Proposals No. 2017B0078, No. 2018A0078, No. 2018B0078, No. 2019A0159, No. 2021A1744). Dr. Lennard Krause, Kasper Tolborg, Kristoffer A. U. Holm are thanked for assistance during beamtimes. We thank Dr. Hazel Reardon for helping us with TGA/DSC measurements.

## Conflict of Interest

The authors declare no conflict of interest.

## Data Availability Statement

The data that support the findings of this study are available from the corresponding author upon reasonable request.

**Keywords:** Chemical Bonding · Doping · Electron Density · Melting · Metal–Organic Frameworks

- [1] a) H. Furukawa, K. E. Cordova, M. O’Keeffe, O. M. Yaghi, *Science* **2013**, *341*, 1230444; b) V. Guillermin, D. Kim, J. F. Eubank, R. Luebke, X. Liu, K. Adil, M. S. Lah, M. Eddaoudi, *Chem. Soc. Rev.* **2014**, *43*, 6141.
- [2] T. D. Bennett, A. K. Cheetham, *Acc. Chem. Res.* **2014**, *47*, 1555.
- [3] C. Orellana-Tavra, E. F. Baxter, T. Tian, T. D. Bennett, N. K. H. Slater, A. K. Cheetham, D. Fairen-Jimenez, *Chem. Commun.* **2015**, *51*, 13878.
- [4] X. Wu, H. Yue, Y. Zhang, X. Gao, X. Li, L. Wang, Y. Cao, M. Hou, H. An, L. Zhang, S. Li, J. Ma, H. Lin, Y. Fu, H. Gu, W. Lou, W. Wei, R. N. Zare, J. Ge, *Nat. Commun.* **2019**, *10*, 5165.
- [5] J. Fonseca, S. Choi, *Dalton Trans.* **2021**, *50*, 3145.
- [6] a) T. D. Bennett, A. L. Goodwin, M. T. Dove, D. A. Keen, M. G. Tucker, E. R. Barney, A. K. Soper, E. G. Bithell, J.-C. Tan, A. K. Cheetham, *Phys. Rev. Lett.* **2010**, *104*, 115503; b) T. D. Bennett, P. Simoncic, S. A. Moggach, F. Gozzo, P. Macchi, D. A. Keen, J.-C. Tan, A. K. Cheetham, *Chem. Commun.* **2011**, *47*, 7983.
- [7] C. Healy, K. M. Patil, B. H. Wilson, L. Hermanspahn, N. C. Harvey-Reid, B. I. Howard, C. Kleinjan, J. Kolien, F. Payet, S. G. Telfer, P. E. Kruger, T. D. Bennett, *Coord. Chem. Rev.* **2020**, *419*, 213388.
- [8] a) T. D. Bennett, S. Horike, *Nat. Rev. Mater.* **2018**, *3*, 431; b) N. Ma, S. Horike, *Chem. Rev.* **2022**, *122*, 4163.
- [9] a) Y. Wang, H. Jin, Q. Ma, K. Mo, H. Mao, A. Feldhoff, X. Cao, Y. Li, F. Pan, Z. Jiang, *Angew. Chem. Int. Ed.* **2020**, *59*, 4365; *Angew. Chem.* **2020**, *132*, 4395; b) L. Frenzel-Beyme, M. Kloß, P. Kolodzeiski, R. Pallach, S. Henke, *J. Am. Chem. Soc.* **2019**, *141*, 12362.

- [10] C. Zhou, L. Longley, A. Krajnc, G. J. Smales, A. Qiao, I. Erucar, C. M. Doherty, A. W. Thornton, A. J. Hill, C. W. Ashling, O. T. Qazvini, S. J. Lee, P. A. Chater, N. J. Terrill, A. J. Smith, Y. Yue, G. Mali, D. A. Keen, S. G. Telfer, T. D. Bennett, *Nat. Commun.* **2018**, *9*, 5042.
- [11] M. A. Ali, J. Ren, T. Zhao, X. Liu, Y. Hua, Y. Yue, J. Qiu, *ACS Omega* **2019**, *4*, 12081.
- [12] M. A. Ali, X. Liu, Y. Li, J. Ren, J. Qiu, *Inorg. Chem.* **2020**, *59*, 8380.
- [13] G. Jiang, C. Ou, F. Xu, E. Zhang, Q. Lu, X. Cai, S. Hausdorf, H. Wang, S. Kaskel, *Adv. Funct. Mater.* **2021**, *31*, 2104300.
- [14] C. Gao, Z. Jiang, S. Qi, P. Wang, L. R. Jensen, M. Johansen, C. K. Christensen, Y. Zhang, D. B. Ravnsbæk, Y. Yue, *Adv. Mater.* **2022**, *34*, 2110048.
- [15] R. Lin, X. Li, A. Krajnc, Z. Li, M. Li, W. Wang, L. Zhuang, S. Smart, Z. Zhu, D. Appadoo, J. R. Harmer, Z. Wang, A. G. Buzanich, S. Beyer, L. Wang, G. Mali, T. D. Bennett, V. Chen, J. Hou, *Angew. Chem. Int. Ed.* **2022**, *61*, e202112880; *Angew. Chem.* **2022**, *134*, e202112880.
- [16] R. N. Widmer, G. I. Lampronti, B. Kunz, C. Battaglia, J. H. Shepherd, S. A. T. Redfern, T. D. Bennett, *ACS Appl. Nano Mater.* **2018**, *1*, 497.
- [17] T. D. Bennett, J.-C. Tan, Y. Yue, E. Baxter, C. Ducati, N. J. Terrill, H. H. M. Yeung, Z. Zhou, W. Chen, S. Henke, A. K. Cheetham, G. N. Greaves, *Nat. Commun.* **2015**, *6*, 8079.
- [18] R. Gaillac, P. Pullumbi, K. A. Beyer, K. W. Chapman, D. A. Keen, T. D. Bennett, F.-X. Coudert, *Nat. Mater.* **2017**, *16*, 1149.
- [19] R. Gaillac, P. Pullumbi, F.-X. Coudert, *J. Phys. Chem. C* **2018**, *122*, 6730.
- [20] T. D. Bennett, D. A. Keen, J.-C. Tan, E. R. Barney, A. L. Goodwin, A. K. Cheetham, *Angew. Chem. Int. Ed.* **2011**, *50*, 3067; *Angew. Chem.* **2011**, *123*, 3123.
- [21] a) L. Frentzel-Beyme, M. Kloß, R. Pallach, S. Salamon, H. Moldenhauer, J. Landers, H. Wende, J. Debus, S. Henke, *J. Mater. Chem. A* **2019**, *7*, 985; b) J. Hou, M. L. Ríos Gómez, A. Krajnc, A. McCaul, S. Li, A. M. Bumstead, A. F. Sapnik, Z. Deng, R. Lin, P. A. Chater, D. S. Keeble, D. A. Keen, D. Appadoo, B. Chan, V. Chen, G. Mali, T. D. Bennett, *J. Am. Chem. Soc.* **2020**, *142*, 3880; c) R. S. K. Madsen, S. Sarkar, B. B. Iversen, Y. Yue, *Chem. Commun.* **2022**, *58*, 823.
- [22] K. Tolborg, B. B. Iversen, *Chem. Eur. J.* **2019**, *25*, 15010.
- [23] a) R. D. Poulsen, A. Bentien, T. Graber, B. B. Iversen, *Acta Crystallogr. Sect. A* **2004**, *60*, 382; b) R. D. Poulsen, M. R. V. Jørgensen, J. Overgaard, F. K. Larsen, W. Morgenroth, T. Graber, Y.-S. Chen, B. B. Iversen, *Chem. Eur. J.* **2007**, *13*, 9775; c) H. F. Clausen, J. Overgaard, Y. S. Chen, B. B. Iversen, *J. Am. Chem. Soc.* **2008**, *130*, 7988.
- [24] N. K. Hansen, P. Coppens, *Acta Crystallogr. Sect. A* **1978**, *34*, 909.
- [25] C. Zhou, M. Stepniewska, J. M. Sørensen, L. Scarpa, G. Magnacca, V. Boffa, T. D. Bennett, Y. Yue, *Microporous Mesoporous Mater.* **2018**, *265*, 57.
- [26] M. J. Turner, J. J. McKinnon, D. Jayatilaka, M. A. Spackman, *CrystEngComm* **2011**, *13*, 1804.
- [27] Deposition Numbers 2126088, 2126093, 2126142, 2126143, 2126144, 2126145, 2126146, 2126150, 2126151, 2126152, 2126153 and 2126154 contain the supplementary crystallographic data for this paper. These data are provided free of charge by the joint Cambridge Crystallographic Data Centre and Fachinformationszentrum Karlsruhe Access Structures service.
- [28] R. F. W. Bader, *Atoms in Molecules. A Quantum Theory*, Clarendon Press, Oxford, New York, **1990**.
- [29] P. Macchi, A. Sironi, *Coord. Chem. Rev.* **2003**, *238–239*, 383.
- [30] C. Gatti, *Z. Kristallogr. Cryst. Mater.* **2005**, *220*, 399.
- [31] H. Kasai, K. Tolborg, M. Sist, J. Zhang, V. R. Hathwar, M. Ø. Filsø, S. Cenedese, K. Sugimoto, J. Overgaard, E. Nishibori, B. B. Iversen, *Nat. Mater.* **2018**, *17*, 249.
- [32] J. Zhang, L. Song, M. Sist, K. Tolborg, B. B. Iversen, *Nat. Commun.* **2018**, *9*, 4716.
- [33] K. Tolborg, B. B. Iversen, *Chem. Mater.* **2021**, *33*, 5308.
- [34] N. Lock, Y. Wu, M. Christensen, L. J. Cameron, V. K. Peterson, A. J. Bridgeman, C. J. Kepert, B. B. Iversen, *J. Phys. Chem. C* **2010**, *114*, 16181.
- [35] C. Wu, D. Xie, Y. Mei, Z. Xiu, K. M. Poduska, D. Li, B. Xu, D. Sun, *Phys. Chem. Chem. Phys.* **2019**, *21*, 17571.
- [36] S. Hashimoto, K. Ono, H. Takeuchi, I. Harada, *Spectrochim. Acta Part A* **1994**, *50*, 1647.

Manuscript received: February 19, 2022

Accepted manuscript online: March 14, 2022

Version of record online: March 29, 2022